JOURNAL OF SYNCHROTRON RADIATION
ISSN 1600-5775

Elemental fingerprinting of mineral species in iron-fortified milk: anomalous small-angle X-ray scattering and resonant soft X-ray scattering studies

Bridget Ingham,[a]* Nigel Kirby,[b] Cheng Wang,[c] Mike Brady[c] and Alistair Carr[d]

[a]Callaghan Innovation, PO Box 31-310, Lower Hutt 5040, New Zealand, [b]Australian Synchrotron, 800 Blackburn Road, Clayton, VIC 3168, Australia, [c]Advanced Light Source, Lawrence Berkeley National Laboratory, Berkeley, CA 94720, USA, and [d]School of Food and Nutrition, Massey University, Private Bag 11222, Palmerston North 4442, New Zealand. *Correspondence e-mail: bridget.ingham@callaghaninnovation.govt.nz

Received 19 February 2018
Accepted 24 May 2018

Edited by V. Favre-Nicolin, CEA and Université Joseph Fourier, France

Keywords: anomalous small-angle X-ray scattering; resonant soft X-ray scattering; milk; iron fortification.

Supporting information: this article has supporting information at journals.iucr.org/s

Anomalous small-angle X-ray scattering (ASAXS) and resonant soft X-ray scattering (RSoXS) are two related techniques that can enable element-specific structural information to be obtained. The development of iron-fortified milk products can greatly benefit from such techniques, allowing the structure of iron and other minerals (such as native calcium) within the casein micelle to be determined. Each method has advantages and disadvantages: for ASAXS, the sample preparation is straightforward, but the signal is relatively low and information about the structure of Ca is difficult to access. RSoXS can be used to study both Ca and Fe, and the element-specific signals observed are proportionally much higher; however, the measurements are challenging due to the difficulty of precise control of the solution thickness using currently available vacuum-compatible liquid cells. Nevertheless, complementary results from both techniques indicate Fe is co-located with Ca, *i.e.* within the colloidal calcium phosphate nanoclusters that are present within native casein micelles in milk.

1. Introduction

Milk and milk products (*e.g.* yoghurt, cheese) are used globally as important food systems for delivering dietary calcium and other minerals. Calcium is present in relatively high concentrations in milk through being encapsulated in casein micelles: approximately spherical protein aggregates several hundred nanometres in size. Within the micelles, calcium binds with phosphate and other counterions to phosphoserine (SerP) groups on the casein proteins. The inorganic species form small clusters 2–3 nm in size, termed colloidal calcium phosphate (CCP) (Dalgleish, 2011).

CCP can also incorporate other divalent species such as Fe, Cu, Zn and Mg when they are added to milk (Philippe *et al.*, 2005). Iron is a vital mineral that can be incorporated into CCP, resulting in easily digestible dairy products that could help mitigate iron-deficiency disorders such as anaemia (Raouche *et al.*, 2009). Fe binds to the SerP sites (Gaucheron, 2000) with greater affinity than Ca (Philippe *et al.*, 2005), but does not cause the micelle size to change significantly (Gaucheron *et al.*, 1997). It is therefore expected that Fe is localized at the CCP particles.

Elemental analysis reveals that over 98% of the added Fe is bound within the casein micelles (Philippe *et al.*, 2005). To investigate the location of Fe within the micelle, structural analysis methods specific to Fe, and ideally also Ca, are required. X-ray absorption near-edge spectroscopy (XANES) has previously been used to obtain short-range structural

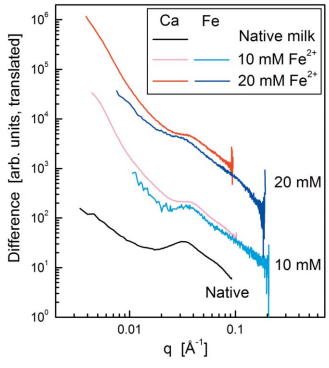

information about calcium in native milk, and showed that it is similar to brushite (Holt *et al.*, 1982). However, the structural information offered by X-ray absorption spectroscopy is limited to the immediate co-ordination sphere [in the case of XANES; extended X-ray absorption fine structure (EXAFS) may provide information out to the second and third nearest neighbours in a well ordered system, but no such results have been reported in the literature for Ca or other species in milk].

In small-angle neutron scattering (SANS), contrast variation has been used for many years to investigate the structure of casein micelles in milk (Stothart & Cebula, 1982; Hansen *et al.*, 1996; Holt *et al.*, 2003; De Kruif *et al.*, 2012; De Kruif, 2014; Bouchoux *et al.*, 2015). In this technique, the milk is reconstituted in a mixed H_2O/D_2O solvent, where the H_2O/D_2O ratio is chosen to have a neutron scattering length that matches that of one part of the system, *e.g.* protein. Since the scattering intensity from each component is proportional to the square of the scattering length contrast, that component is rendered invisible to neutrons. Measurements performed at the protein match point (corresponding to approximately 40% D_2O) show a feature presumed to correspond to CCP (Holt *et al.*, 2003; De Kruif *et al.*, 2012; De Kruif, 2014; Bouchoux *et al.*, 2015). However, this assignment can only be inferred; the measurement is not specific to calcium *per se*.

An analogous technique using X-rays can provide element-specific structural information. Here, contrast variation is provided through changing the incident X-ray wavelength (or photon energy) and comparing measurements made in the vicinity of an absorption edge of the element of interest. In the hard X-ray region ($E > 4$ keV) the technique is commonly called anomalous small-angle X-ray scattering (ASAXS), while in the soft X-ray region ($E < 4$ keV) it is called resonant soft X-ray scattering (RSoXS), since in this energy range the scattering angles are no longer 'small' due to the longer wavelength. The atomic scattering factor for X-rays can be written as $f(q, E) = f_0(q) + f'(E) + if''(E)$, where f_0 is the (energy-independent) normal scattering, roughly proportional to the number of electrons; $f'(E)$ is the atomic dispersion term and $f''(E)$ is the atomic absorption term. Near an absorption edge, $f'(E)$ and $f''(E)$ vary significantly. The difference in overall scattering intensity is therefore related to objects containing the target element.

In our earlier work, RSoXS measurements of native cow milk at the Ca $L_{2,3}$-edge enabled a positive identification of the CCP signal (Ingham *et al.*, 2015, 2016). The CCP scattering feature was found to have a different shape and position to most other reports based on SAXS data, but was consistent with SANS results. The discrepancy with the SAXS data can be ascribed to a misinterpretation by other authors as to the identity of the main feature at higher q. This feature is commonly attributed to the CCP form factor; however, it is much more likely to be scattering due to local density fluctuations in the protein structure (De Kruif *et al.*, 2012; De Kruif, 2014; Ingham *et al.*, 2016). Here we show the application of RSoXS to iron-fortified cow milk (with 10 or 20 m*M* added Fe^{2+}) at both the Ca and Fe $L_{2,3}$-edges and compare the results with ASAXS at the Fe *K*-edge, to obtain structural information about both Ca and Fe in iron-fortified milk and to demonstrate the applicability and limitations of the two techniques.

2. Experimental

2.1. Preparation of milk solutions

Cow skim milk powder was obtained from Fonterra Co-operative (purchased from Milligans Food Group Ltd, Oamaru, New Zealand) and was reconstituted in MilliQ water in a 3.5 wt% protein concentration (1:10 total weight) with 0.2 wt% sodium azide. 0.2 *M* $FeSO_4$ was added to milk at 4°C to give an overall Fe^{2+} concentration of 10 or 20 m*M*, and the pH was readjusted to 6.7 using 0.5 *M* NaOH solution.

2.2. Anomalous small-angle X-ray scattering (ASAXS)

Small-angle X-ray scattering (SAXS) measurements were performed at the Australian Synchrotron SAXS beamline (Kirby *et al.*, 2013) at two X-ray energies near the Fe *K*-edge: 7000 eV (off-resonance) and 7107 eV (on-resonance). Samples were measured at a temperature of 4°C using a flowing capillary setup, with twenty 1 s exposures being collected using a Pilatus 1M detector, summed and radially averaged. The capillary was 2 mm in diameter. Water backgrounds were collected in the same capillary before and after each measurement to check for radiation-induced fouling of the walls; no significant fouling was observed. Due to the high accuracy of the scattering intensity values required and the possibility of the scattering being time-dependent (Ingham *et al.*, 2016), four measurements were performed for each sample: two at 7107 eV, one at 7000 eV, followed by an additional measurement at 7107 eV. The averaged data at 7107 eV were interpolated in time, point-by-point, to provide a pattern corresponding to the exact time when the 7000 eV measurement was made. The difference between the first and last measurements collected at 7107 eV was around 3–4%, which, for the 10 m*M* sample, is comparable with the differences between the 7000 eV measurement and the time-interpolated 7107 eV measurement (4–5%). The energy range of the Australian Synchrotron SAXS beamline does not extend to the Ca *K*-edge (4080 eV).

2.3. Resonant soft X-ray scattering (RSoXS)

RSoXS measurements were performed at beamline 11.0.1.2 at the Advanced Light Source, Lawrence Berkeley National Laboratory, USA (Gann *et al.*, 2012) over two energy ranges: 347–355 eV in 0.2 eV steps, encompassing the Ca L_2 and L_3 absorption edges; and 705–715 eV in 0.5 eV steps, covering the Fe L_2 and L_3 absorption edges. Measurement times varied between 1 and 10 s depending on X-ray energy and sample thickness. The scattered X-rays were collected using a CCD detector. To reduce scattering and absorption of the X-rays by air, the entire sample and detector arrangement was housed in a high-vacuum chamber. The liquid samples were mounted by sandwiching a small drop between two silicon nitride windows, which were then sealed with epoxy. Each window was 1 mm ×

1 mm in size and 100 nm thick, with a 1 µm SU-8 spacer deposited on one of the window frames. Samples were mounted and transported on a chilled aluminium block. The sample holder on the beamline was chilled to 5°C during the vacuum pump-down and measurements.

2.4. Data analysis

The scattering equation involves the atomic scattering term $|f(q,E)|^2$, which shows negligible energy-dependence far from an absorption edge, but near an edge the dispersion and absorption terms become significant. For a material comprising two kinds of scattering objects, one consisting of the resonant element and the other not, the scattering pattern from the former can be isolated from the resonant component. Using the notation of Ballauff & Jusufi (2006), the intensity is

$$I_S(q,E) = F_0(q)^2 + 2F_0(q)\,v(q)\,f'(E) + v(q)^2\left[f'(E)^2 + f''(E)^2\right], \quad (1)$$

where $F_0(q)$ is the non-resonant scattering amplitude (*i.e.* total scattering from non-resonant objects, plus non-resonant scattering from the resonant objects), $v(q)$ is the scattering amplitude from the resonant objects, and $f'(E)$ and $f''(E)$ are the atomic dispersion and absorption terms (Ballauff & Jusufi, 2006), tabulated by Henke *et al.* (1993). This expression is completely general and applies to both hard and soft X-ray resonance effects.

The first term, $F_0(q)^2$, is the non-resonant scattering intensity. The difference in intensity between measurements performed at two energies comprises the last term, $v(q)^2[f'(E)^2 + f''(E)^2]$, which is purely resonant scattering, and the central term, $2F_0(q)\,v(q)\,f'(E)$, which is mixed. The mixed term can be isolated by measuring the scattering intensity at at least one additional energy below the absorption edge, and knowing or measuring $f'(E)$ and $f''(E)$. These can be obtained experimentally from X-ray absorption spectroscopy measurements, since $f''(E)$ is the absorption, and applying a Kramers–Kronig transformation to obtain $f'(E)$ (Stuhrmann, 2007). However, in practise it is not always possible to perform these measurements. In cases where the scattering feature involving the target species is located in a q-range sufficiently far removed from other non-resonant scattering features, qualitative information about the resonant scattering feature (position and shape, but not absolute intensity) can be obtained by simply taking the difference pattern between two measurements performed at different energies below the absorption edge (Vogtt *et al.*, 2013). This has been demonstrated for systems such as small metal nanoparticles attached to support materials having a much larger particle or pore size (Vogtt *et al.*, 2013; Yu *et al.*, 2009; Jeng *et al.*, 2007; Brumberger *et al.*, 2005).

Given that the exact composition of CCP is unknown (being an amorphous collection of calcium, phosphate, citrate and other ionic species), it is not possible for us to obtain fully quantitative information in the milk system. Since the focus of the work is on the location of the iron, qualitative structural information is sufficient. The two main scattering objects in the system are the CCP particles and the casein micelles, which are sufficiently different in size. Therefore, we used the simplified analysis method by subtracting one dataset from another (with both datasets normalized to the incident beam intensity). At the Fe *K*-edge, the scattering intensity decreases slightly, so the difference pattern was obtained from $I(q, 7000\text{ eV}) - I(q, 7107\text{ eV})$. At the Ca and Fe *L*-edges, the scattering intensity increases, with maxima at 349.2 eV (Ca) and 708 eV (Fe), so the difference patterns were obtained from $I(q, 349.2\text{ eV}) - I(q, 347\text{ eV})$ for Ca and $I(q, 708\text{ eV}) - I(q, 706\text{ eV})$ for Fe.

3. Results

3.1. ASAXS

The off-resonance (normal) SAXS curves for milk with 10 m*M* and 20 m*M* Fe^{2+} added are shown in Fig. 1, together with the anomalous signal, obtained by subtracting the on-

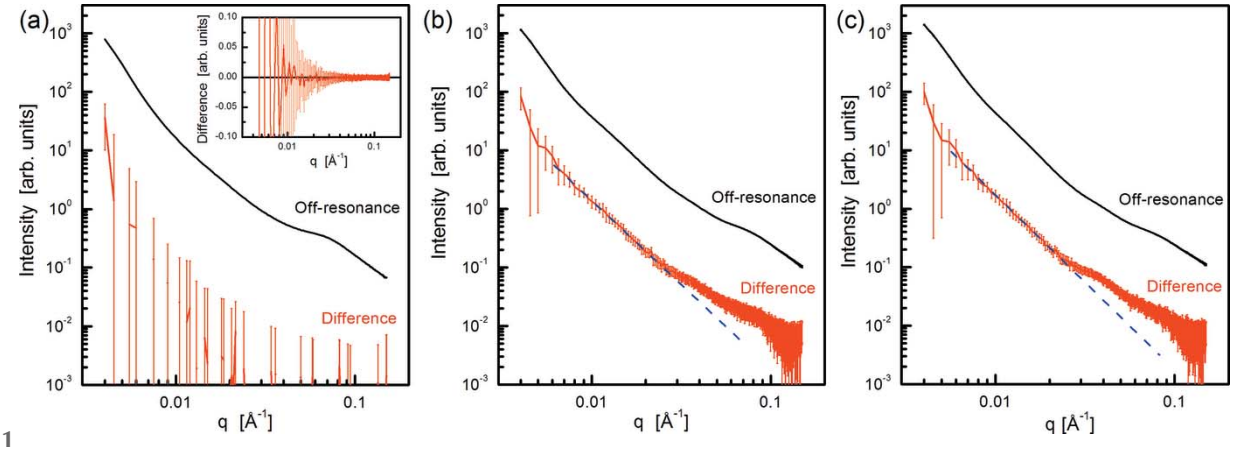

Figure 1
Normal (off-resonance) scattering (black lines) and anomalous scattering component (red lines) near the Fe *K*-edge for milk to which $FeSO_4$ was added in concentrations of (*a*) 0 m*M*, (*b*) 10 m*M*, (*c*) 20 m*M*. The dashed blue lines in (*b*) and (*c*) are given as guides to the eye, highlighting the deviation of the anomalous scattering at q = 0.035 Å^{-1}, corresponding to CCP. The inset in (*a*) shows the difference intensity on a linear scale, demonstrating negligible difference between the on- and off-resonance scattering.

resonance SAXS from the off-resonance SAXS. For comparison, data from the same measurements are shown for native milk (*i.e.* no Fe^{2+} added); as expected, no anomalous signal was detected. For the milk with Fe^{2+} added, both the normal and difference curves [$I(q, 7000\ \text{eV}) - I(q, 7107\ \text{eV})$] are similar for the two concentrations. The normal curves show four regions, described in our earlier work (Ingham *et al.*, 2016) as follows: low q, corresponding to scattering from the overall micelle; a shoulder centred around $q = 0.01$ Å^{-1}, corresponding to internal structures within the micelle ['incompressible regions' divided by water channels (Bouchoux *et al.*, 2015)]; a small feature around $q = 0.035$ Å^{-1}, corresponding to the CCP separation; and a slightly more pronounced feature around $q = 0.08$ Å^{-1}, corresponding to protein inhomogeneities (De Kruif *et al.*, 2012). The anomalous components (difference curves) show power-law scattering, arising from the micelle, and a feature centred around $q = 0.035$ Å^{-1}. Blue dashed lines in Fig. 1 help to illustrate the magnitude of this feature. The signal for the 20 m*M* Fe milk sample is approximately double that of the 10 m*M*, and is more evident than the corresponding feature in the normal scattering curve in both cases. In addition, the feature located at $q = 0.08$ Å^{-1} in the normal scattering is not evident in the difference curves, although given the large uncertainties its absence is inconclusive. It should also be noted that the difference curves in Fig. 1 have not been scaled; the resonant component is approximately an order of magnitude smaller than the normal scattering. This is reflected by the proportionally larger error bars shown on the difference data curves.

3.2. RSoXS

In contrast to the ASAXS data, where the magnitude of the resonant signal is 10% or less of the normal signal, and the total intensity decreases approaching the absorption edge, RSoXS data show a significant enhancement by up to ten-fold at the absorption edge. Scattering patterns collected at selected energies are shown in Fig. 2 for milk samples prepared in the same way (10 m*M* and 20 m*M* Fe^{2+} added to milk). At the Ca $L_{2,3}$-edge the signal at $q = 0.035$ Å^{-1} increases dramatically (Figs. 2*a*, 2*d*). At the Fe $L_{2,3}$-edge the increase is small, on top of a large background (Figs. 2*b*, 2*e*) but has the characteristic appearance of Fe^{2+} (Koehl *et al.*, 2013).

The anomalous contribution is estimated by subtracting the off-resonance SAXS data from the on-resonance. This was performed for data collected at both the Ca and Fe edges [$I(q, 349.2\ \text{eV}) - I(q, 347\ \text{eV})$ for Ca and $I(q, 708\ \text{eV}) - I(q, 706\ \text{eV})$ for Fe], and is shown in Fig. 3, along with Ca edge data for native milk (Ingham *et al.*, 2015). For the milk with 10 m*M* added Fe^{2+}, the curves have virtually identical shapes

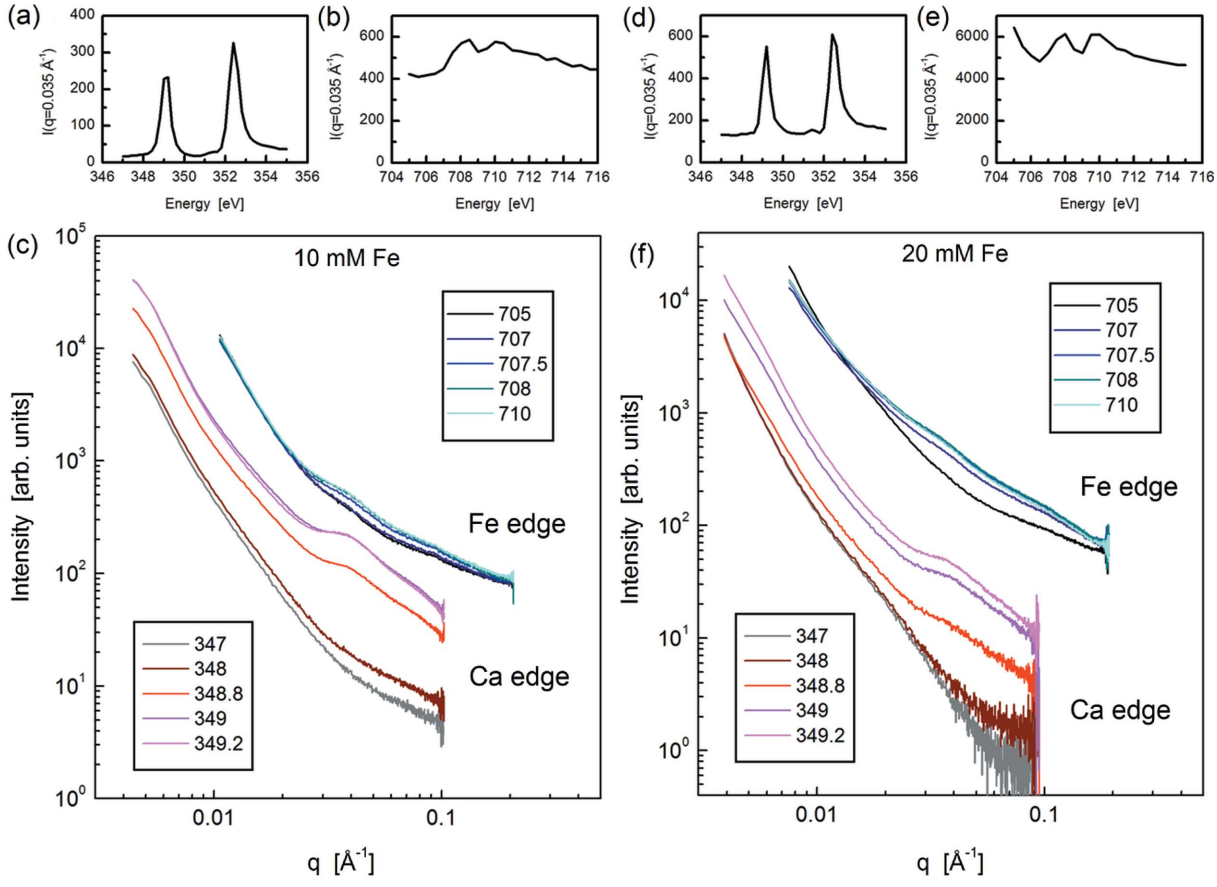

Figure 2
Resonant soft X-ray scattering data for milk to which $FeSO_4$ was added in concentrations of 10 m*M* (left) and 20 m*M* (right). Also shown are plots of the intensity at $q = 0.035$ Å^{-1} at energies spanning the Ca $L_{2,3}$-edge (*a*, *d*) and the Fe $L_{2,3}$-edge (*b*, *e*). The raw data (*c*, *f*) are shown for selected energies as labelled.

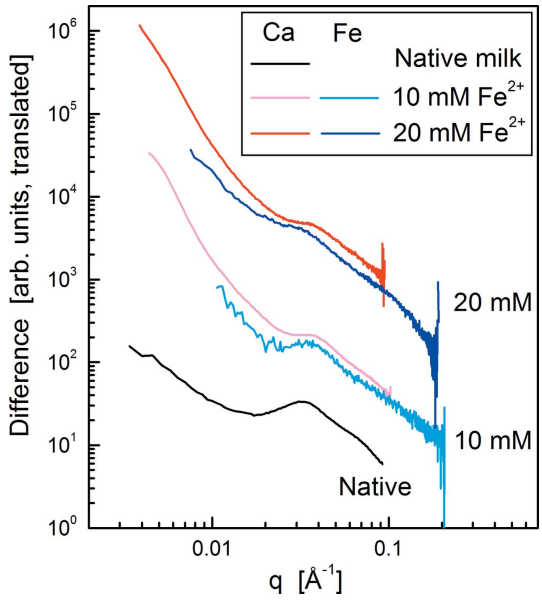

Figure 3
RSoXS difference plots (on-resonance minus off-resonance) at the Ca and Fe $L_{2,3}$-edges of cow milk with 0, 10 and 20 m*M* Fe^{2+} added.

at both the Ca and Fe edges. They are also similar to the native milk in shape and position of the main features. In our earlier work on native milk, the Ca resonant feature was fitted to a population of spheres with hard sphere structure factor, representing the CCP particles within the casein micelle (Ingham *et al.*, 2015). Since the 10 m*M* data at both the Ca and Fe edges have the same shape, we can conclude that the Fe is co-located with the Ca at the CCP particles.

For the 20 m*M* data, the corresponding feature occurs at the same q value as the native and 10 m*M* samples for the Ca edge, while at the Fe edge it occurs at slightly lower q, which would normally be interpreted as the Fe-containing objects being further apart at the higher concentration. However, this is not possible if in fact the Fe is co-located with Ca at the CCP particles. It must be noted that, particularly at the Fe L-edge, there can be considerable variation in the magnitude and shape of the resonant scattering feature. This will be discussed shortly; the data shown in Fig. 3 have been selected based on their scattering to fluorescence ratio being closest to optimum.

4. Discussion

In the soft X-ray region, absorption, scattering and fluorescence occur from virtually all elements present in the system. The cross-sections (*i.e.* relative probabilities) of these are tabulated (Henke *et al.*, 1993; Hubbell *et al.*, 1975, 1982). The probability that a fluorescence photon will be emitted is the product of the photon absorption cross-section τ and the fluorescence yield ω_K (the probability that a fluorescence photon, rather than an Auger electron, will be emitted). ω_K values are also tabulated (Krause, 1979). There is little difference in the scattering cross-sections between the Ca and Fe L-edges (350 eV and 710 eV); however, there are significant differences in the absorption, particularly for oxygen, which has an absorption edge at 540 eV. We hypothesize that the increased background in the Fe data (Fig. 2) is primarily due to fluorescence from the oxygen present in the water molecules, and that this is significant compared with the resonant signal.

The incident, scattered and fluorescence photons can all be absorbed by the sample. Assuming no double scattering events, for a section of sample of thickness dt, this can be expressed as

$$\mathrm{d}I = I_0 \exp(-\alpha_0 t)\left\{I_S(q, E)\exp\left[-\alpha_0(t_s - t)\right] + I_F(q, E)\exp\left[-\alpha_f(t_s - t)\right]\right\}\mathrm{d}t$$

where I_0 is the incident beam intensity, t_s is the total sample thickness, α_0 is the absorption length of photons of incident energy E_0, $I_S(q, E)$ is the scattering intensity, $I_F(q, E)$ is the fluorescence intensity, and α_f is the absorption length of photons of the fluorescence energy E_f.

The total signal is then

$$I = \int_0^{t_s} I_0 \exp(-\alpha_0 t)\left\{I_S(q, E)\exp\left[-\alpha_0(t_s - t)\right] + I_F(q, E)\exp\left[-\alpha_f(t_s - t)\right]\right\}\mathrm{d}t$$

which becomes

$$I = I_0 I_S(q, E)\, t_s \exp(-\alpha_0 t_s) + I_0 I_F(q, E)\,\frac{\exp(-\alpha_0 t_s) - \exp(\alpha_f t_s)}{\alpha_f - \alpha_0}. \quad (2)$$

Since each element has a different characteristic fluorescence energy, α_f will be different for each. The fluorescence intensities must therefore be scaled according to the number of atoms present and the second term is replaced by a sum over each species,

$$I_F(q, E) = I_0 \textstyle\sum_i c_i I_{Fi}(q, E)\,\dfrac{\exp(-\alpha_0 t_s) - \exp(\alpha_{f,i} t_s)}{\alpha_{f,i} - \alpha_0}. \quad (3)$$

In equation (3), c_i is the atomic fraction of element i and $I_{Fi}(E) \propto \tau_i \omega_{Ki}$. The absorption length α is given by $\alpha = 2r_e\lambda/Am_u f''(E)$, where r_e is the radius of the electron (2.82×10^{-13} cm), λ is the X-ray wavelength, A is the number of atomic mass units, m_u is the atomic mass unit (1.661×10^{-24} g) and $f''(E)$ is the resonant atomic absorption term (Attwood, 1999).

Tables SI–SVI of the supporting information give the calculation of relative fluorescence signals for a 1 µm-thick milk solution sample containing 10 m*M* Fe, sandwiched between two 100 nm-thick silicon nitride windows, and measured at the Ca and Fe $L_{2,3}$-edges. In our measurements, the actual solution thickness could not be accurately controlled and was likely to have been in the range 1–5 µm.

The calculated fluorescence signals at the Ca and Fe edges are shown as a function of solution thickness in Fig. 4. Since the fluorescence at the Fe edge arises mainly from oxygen atoms present in the water molecules, the Fe concentration makes little difference. The fluorescence at the Fe edge is

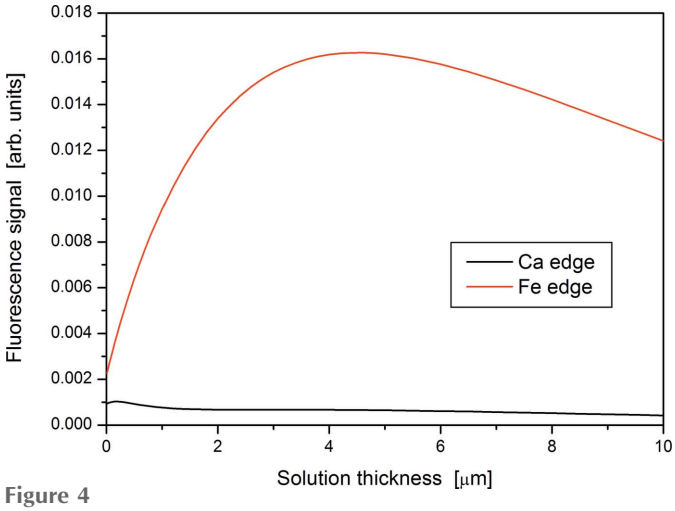

Figure 4
Calculated fluorescence intensity as a function of solution thickness for milk solutions with 10 m*M* Fe, sandwiched between two 100 nm-thick silicon nitride windows, in the vicinity of the Ca $L_{2,3}$-edge at 350 eV and the Fe $L_{2,3}$-edge at 710 eV.

20–25 times that at the Ca edge for solution thicknesses in the 1–5 μm range. The optimum solution thickness for minimizing the fluorescence at the Fe edge is <2 μm.

These effects are evident in our experimental results. At the Ca edge, the resonant scattering is clearly observed in almost every instance, reaching a maximum of around ten times the non-resonant scattering intensity at q = 0.035 Å^{-1}. The fluorescence signal is relatively minor in comparison. If we estimate the fluorescence signal to be around half that of the non-resonant scattering at the Ca edge, then at the Fe edge this would rise to ten times the non-resonant scattering and be on par with the resonant scattering signal.

During our experiments, measurements of the 10 m*M* Fe-added milk sample were repeated numerous times, with each one mounted between new windows. Eight of these measurements at the Ca and Fe $L_{2,3}$-edges are shown in Fig. 5 for both the resonant component (difference plot) and the normal/off-resonance scattering. (Sample 4 was chosen as the clearest result, displayed in Figs. 2 and 3.) There is a high degree of variability between the various measurements. At the Ca edge, most of the curves exhibit a resonant feature at q = 0.035 Å^{-1} (red lines in Fig. 5). The consistency of this feature allows us to be confident that the Ca within the CCP is unchanged from the native system. However, at the Fe edge, the shape and intensity of the resonant curves is highly variable (blue lines). Only two of the resonant curves show a clear resonant feature at q = 0.035 Å^{-1}; samples 4 and 8. These two samples have the lowest intensity in their respective normal scattering plots (green lines), indicating they are likely the thinnest. The other normal scattering curves plateau at high q. This behaviour is symptomatic of a fluorescence signal, which is largely independent of scattering angle. Sample 6, for example, plateaus at a high value and shows a low signal in the difference plot with significant noise. These results demonstrate that, if the sample is too thick, not only the intensity but also the shape of the resonant component of the scattering curve may be compromised. Fewer repeats were performed on the 20 m*M* Fe solution than the 10 m*M* Fe solution; the data shown in Figs. 2 and 3 may have been affected by thickness effects.

The experimental results are consistent with the theoretical predictions in that at the Ca edge the fluorescence is relatively

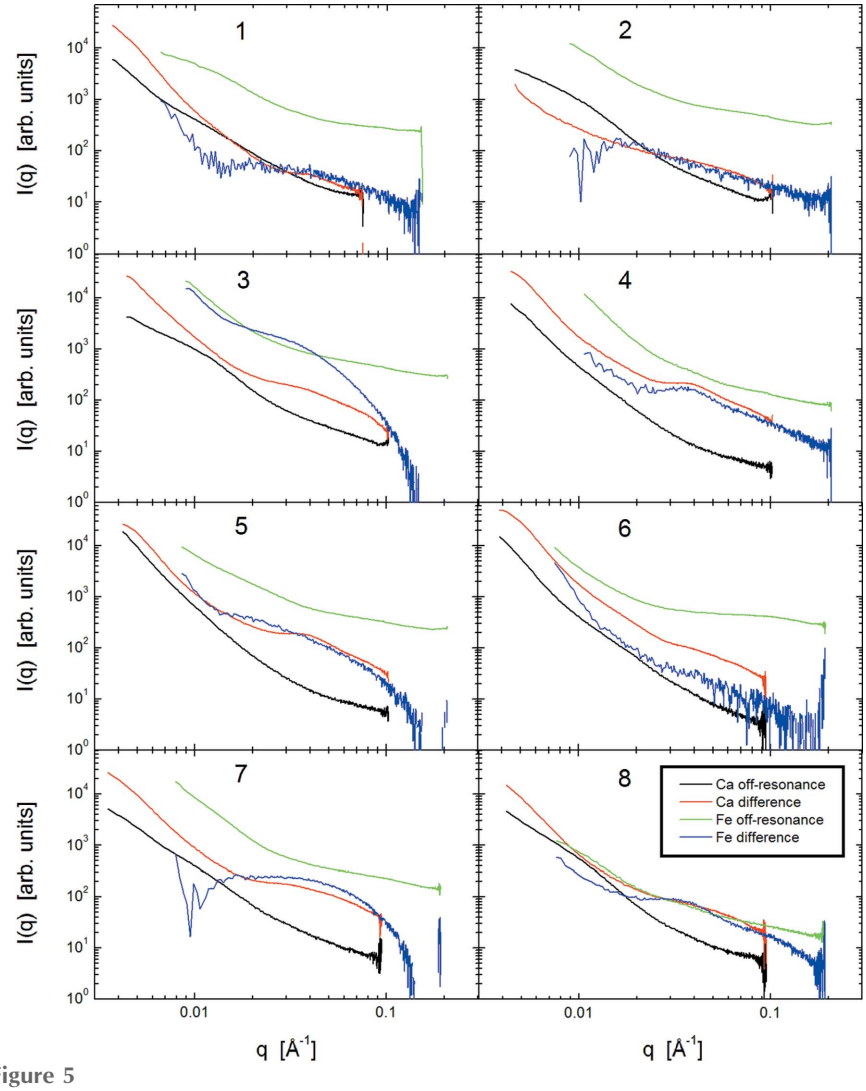

Figure 5
Off-resonance and difference plots at the Ca and Fe edges for eight different samples of milk to which 10 m*M* Fe was added, showing variability between measurements of the same sample in different cells (*i.e.* different solution thicknesses).

low and there is a reasonably wide range of solution thicknesses where the magnitude of the resonant scattering signal (taking absorption into account) is acceptable. This range is much narrower at the Fe edge due to increased fluorescence, primarily from oxygen atoms present in the water, which makes up about 90% by weight.

There is limited scope for optimizing the ratio of resonant scattering to fluorescence at the Fe edge, since to reduce the fluorescence by using thinner samples would also cause a reduction in the scattering intensity due to there being fewer scattering objects in the beam path.

5. Conclusions

ASAXS and RSoXS both show resonance signals at the Fe *K*-edge and *L*-edge, respectively, for Fe fortified milk. RSoXS has the additional advantage of being able to probe for Ca, which is not easily accessible in the ASAXS energy range. The results showed that, for 10 m*M* added Fe, the Fe and Ca signals were similar, indicating that both are co-located in the same structures. For 20 m*M* added Fe, the RSoXS feature at the Ca edge was unchanged while at the Fe edge the feature had moved to lower q. However, it is unclear whether this is a larger spacing of Fe-containing scattering objects or an artefact of solution thickness.

The effect of solution thickness on the fluorescence signal (taking absorption by the solution into account) is described for X-ray energies probed by RSoXS. Fluorescence is significant, particularly above the oxygen edge. At the Fe edge the optimal solution thickness is less than 2 µm. This requires careful control over the solution thickness for these measurements. Future work will focus on combining Ca *L*-edge RSoXS results with Fe *K*-edge ASAXS, as these appear to be the most reliable.

Acknowledgements

Portions of this work were funded by the New Zealand Ministry of Business, Innovation and Employment (MBIE) under contract C08X1003. Catalyst: Seeding funding was provided by the New Zealand Ministry of Business, Innovation and Employment and administered by the Royal Society of New Zealand (contract CSG-CIN1601). Portions of this research were undertaken on the SAXS/WAXS beamline at the Australian Synchrotron, Victoria, Australia, and beamline 11.0.1 at the Advanced Light Source, Berkeley. The Advanced Light Source is supported by the Director, Office of Science, Office of Basic Energy Sciences, of the US Department of Energy under Contract No. DE-AC02-05CH11231. Gad Erlangga and Alice Smialowska prepared solutions for measurements at the Australian Synchrotron and the Advanced Light Source.

Funding information

The following funding is acknowledged: New Zealand Ministry of Business, Innovation and Employment (grant No. C08X1003; grant No. CSG-CIN1601).

References

Attwood, D. T. (1999). *Soft X-rays and Extreme Ultraviolet Radiation*, p. 64. Cambridge University Press.
Ballauff, M. & Jusufi, A. (2006). *Colloid Polym. Sci.* **284**, 1303–1311.
Bouchoux, A., Ventureira, J., Gésan-Guiziou, G., Garnier-Lambrouin, F., Qu, P., Pasquier, C., Pézennec, S., Schweins, R. & Cabane, B. (2015). *Soft Matter*, **11**, 389–399.
Brumberger, H., Hagrman, D., Goodisman, J. & Finkelstein, K. D. (2005). *J. Appl. Cryst.* **38**, 324–332.
Dalgleish, D. G. (2011). *Soft Matter*, **7**, 2265–2272.
De Kruif, C. G. (2014). *J. Appl. Cryst.* **47**, 1479–1489.
De Kruif, C. G., Huppertz, T., Urban, V. S. & Petukhov, A. V. (2012). *Adv. Colloid Interface Sci.* **171–172**, 36–52.
Gann, E., Young, A. T., Collins, B. A., Yan, H., Nasiatka, J., Padmore, H. A., Ade, H., Hexemer, A. & Wang, C. (2012). *Rev. Sci. Instrum.* **83**, 045110.
Gaucheron, F. (2000). *Trends Food Sci. Technol.* **11**, 403–409.
Gaucheron, F., Le Graët, Y., Raulot, K. & Piot, M. (1997). *Int. Dairy J.* **7**, 141–148.
Hansen, S., Bauer, R., Bredsted Lomholt, S., Bruun Quist, K., Skov Pedersen, J. & Mortensen, K. (1996). *Eur. Biophys. J.* **24**, 143–147.
Henke, B. L., Gullikson, E. M. & Davis, J. C. (1993). *At. Data Nucl. Data Tables*, **54**, 181–342.
Henke, B. L., Lee, P., Tanaka, T. J., Shimabukuro, R. L. & Fujikawa, B. K. (1982). *At. Data Nucl. Data Tables*, **27**, 1–144.
Holt, C., de Kruif, C. G., Tuinier, R. & Timmins, P. A. (2003). *Colloids Surf. A Physicochem. Eng. Asp.* **213**, 275–284.
Holt, C., Hasnain, S. S. & Hukins, D. W. L. (1982). *Biochim. Biophys. Acta*, **719**, 299–303.
Hubbell, J. H., Veigele, W. J., Briggs, E. A., Brown, R. T., Cromer, D. T. & Howerton, R. J. (1975). *J. Phys. Chem. Ref. Data*, **4**, 471–538.
Ingham, B., Erlangga, G. D., Smialowska, A., Kirby, N. M., Wang, C., Matia-Merino, L., Haverkamp, R. G. & Carr, A. J. (2015). *Soft Matter*, **11**, 2723–2725.
Ingham, B., Smialowska, A., Erlangga, G. D., Matia-Merino, L., Kirby, N. M., Wang, C., Haverkamp, R. G. & Carr, A. J. (2016). *Soft Matter*, **12**, 6937–6953.
Jeng, U.-S., Lai, Y.-H., Sheu, H.-S., Lee, J.-F., Sun, Y.-S., Chuang, W.-T., Huang, Y.-S. & Liu, D.-G. (2007). *J. Appl. Cryst.* **40**, s418–s422.
Kirby, N. M., Mudie, S. T., Hawley, A. M., Cookson, D. J., Mertens, H. D. T., Cowieson, N. & Samardzic-Boban, V. (2013). *J. Appl. Cryst.* **46**, 1670–1680.
Koehl, A., Kajewski, D., Kubacki, J., Lenser, C., Dittmann, R., Meuffels, P., Szot, K., Waser, R. & Szade, J. (2013). *Phys. Chem. Chem. Phys.* **15**, 8311–8317.
Krause, M. O. (1979). *J. Phys. Chem. Ref. Data*, **8**, 307–327.
Philippe, M., Legraet, Y. & Gaucheron, F. (2005). *Food Chem.* **90**, 673–683.
Raouche, S., Dobenesque, M., Bot, A., Lagaude, A. & Marchesseau, S. (2009). *Eur. Food Res. Technol.* **229**, 929–935.
Stothart, P. H. & Cebula, D. J. (1982). *J. Mol. Biol.* **160**, 391–395.
Stuhrmann, H. B. (2007). *J. Appl. Cryst.* **40**, s23–s27.
Vogtt, K., Goerigk, G., Ballauff, M., Gläser, R. & Dingenouts, N. (2013). *Colloid Polym. Sci.* **291**, 2163–2171.
Yu, C., Koh, S., Leisch, J. E., Toney, M. F. & Strasser, P. (2009). *Faraday Discuss.* **140**, 283–296.